Int. J. Electrochem. Sci., 13 **(2018)** 6388 – 6401, doi: 10.20964/2018.07.58

International Journal of
ELECTROCHEMICAL
SCIENCE
www.electrochemsci.org

Improved Pt/CeO_2 Electrocatalysts for Ethanol Electro-oxidation

Guilherme L. Cordeiro[1], Elaine F. de Camargo[1], Monique C. L. Santos[2], Conrado V. Pereira[2], Valter Ussui[1], Nelson B. de Lima[1], Almir O. Neto[2,], Dolores R. R. Lazar[1]*

[1] Materials Science and Technology Center
[2] Fuel Cells and Hydrogen Center, Energy and Nuclear Research Institute (IPEN-CNEN/SP), Lineu Prestes Avenue, 2242 – Zip Code: 05508-000 – São Paulo, Brazil
[*]E-mail: aolivei@ipen.br

Received: 8 March 2018 / *Accepted:* 28 April 2018 / *Published:* 5 June 2018

A simple and low-cost approach for the preparation of wide-gap (E_g = 3.43 eV), fine cerium dioxide crystals (CeO_2, d = 8.1 nm), was developed in order to support Pt nanoparticles as electrocatalysts for ethanol oxidation. Cerium oxide powders were prepared by precipitation from cerium chloride solution in ammonia medium and the influence of calcination temperature was evaluated. Platinum nanoparticles were incorporated by a wet chemical reduction of chloroplatinic acid with sodium borohydrate. Compared to a state-of-the-art Pt/C, the nanocomposite exhibited a much higher mass activity (2.5×) and significant anti-poisoning ability. The promotional effect of the CeO_2 nanocrystals was discovered to be affected by heat treatment conditions. Compared to oven-dried samples, calcination allows to (i) an enhanced metal–support interaction between CeO_2 and Pt and (ii) an enhancement of electron transportation to catalyst owing to the shrinkage of CeO_2 bandgap, thereby promoting the oxidation of the strongly adsorbed C_xH_y. Therefore, the Pt/CeO_2 nanocomposite appears to be a promising electrocatalyst for advanced energy conversion.

Keywords: Pt/CeO_2 electrocatalysts, semiconductors, crystal growth, bandgap, ethanol oxidation.

1. INTRODUCTION

The ever growing energy pursuit has been challenging industry and government authorities in the whole world. Long-standing promises have considered nuclear power as an attractive option for non-stop and large-scale energy production in our increasingly carbon-constrained world. In recent years, however, interests in decommissioning of nuclear reactors have emerged in the face of the risks of plant failure. Hydroelectric stations, more eco-friendly, are limited to a specific geographical area for the implementation of new facilities, and the availability of decades of cheap fossil fuel energy has been compromised by environmental and political issues. Fuel cells have been generally recognized as

promising low-carbon energy generation systems, which can convert the chemical energy of a fuel directly into electrical energy with low emission of pollutants [1–3].

Basically, proton exchange membrane fuel cells (PEMFCs) can oxidize fuel at the anode and reduce oxygen at the cathode to produce electricity, heat and water. Since hydrogen is presently the most energetic green fuel (33 $kW{\cdot}h{\cdot}kg^{-1}$), it has been considered a promising energy source in PEMFCs [4]. In spite of this, storage and processing challenges have inhibited the consolidation of a hydrogen economy. Compared to the use of hydrogen, liquid alcohols may be easily stored and transported. Therefore, hydrogen-rich alcohols have been investigated as low-carbon energy sources. Ethanol has a quite high energy density (8 $kW{\cdot}h{\cdot}kg^{-1}$), comparable to that of gasoline (10–11 $kW{\cdot}h{\cdot}kg^{-1}$), and the technology needed for its large-scale production has already been established. In addition, it is a low-toxicity, abundant and renewable vector [5,6].

In PEMFCs, fuel oxidation requires highly active catalyst electrodes for boosting conversion efficiencies because of the low operating temperatures (60–120 ºC). So far, it is undisputed that Pt provides the best correlation between exchange current density and fuel binding energy [7]. Despite the superior catalytic activity of Pt, the electro-oxidation of ethanol has been considered one of the most complex fuel cell anode reactions due to the difficulties in breaking the C–C bond and in poisoning by strongly adsorbed species coming from the dissociative adsorption of ethanol [8]. Several attempts, such as the dispersion of Pt on a high-area conductive support [9–14] and its combination with another metal [15–18], have been addressed for solving the catalytic inefficiency topic. Regarding the former approach, it is well-known that suitable fuel cell supports provide high surface-to-volume ratio of metal particles, which, in turn, maximizes the available area for electrocatalytic reactions [19]. In comparison to state-of-the-art carbon materials, metal oxides, such as TiO_2, SiO_2, and Sn-doped In_2O_3, have been used as alternatives of supports in fuel cell reactions. Generally, these inorganic oxides own the main characteristics of an electrode material: nano-sized particulate structure for proper catalyst dispersion, appropriate hydrophilicity for enhancing mass transport, and enhanced oxophilicity for minimizing catalyst poisoning [20,21].

As one of the most reactive rare earth oxides, with a wide bandgap (E_g = 3.15 eV for coarse-grained material) [22], cerium dioxide (ceria, CeO_2) has been mainly used as a promoter in PEMFC applications owing to the coexistence of both Ce^{3+}/Ce^{4+} states. Specifically, the reduction of Ce^{4+} to Ce^{3+} can create oxygen vacancies, as charge compensation defects, that might be capped by other oxidizing species, such as water or even the strongly adsorbed byproducts from reaction itself [23,24]. In view of the oxygen transport properties, cerium oxides have been extensively studied as catalyst promoters. Briefly, and for ease of reference, Fugane [25] examined the microstructure of the Pt–CeO_x ($1.5 < x < 2$) heterointerface in epitaxial-grown films by using cyclic voltammetry in 0.5 $mol{\cdot}L^{-1}$ H_2SO_4 aqueous solution. Their observations indicated that the electrochemical oxidation of Pt was suppressed by the formation of the interface, which enhanced catalyst activity. In related work in terms of the promotional effect of ceria, Yu [26] demonstrated that addition of 20 wt% CeO_2 on Pt/C catalysts could improve the electroactivity for the oxidation of small molecular alcohols (methanol, ethanol, ethylene glycol and glycerol). The promotional effect was attributed to the oxygen-containing species generated by ceria, associated to its high oxygen storage capacity, which accelerated oxidation of byproducts strongly adsorbed on Pt surface. On the basis of this bifunctional effect, or in other

words, the ability to form surface oxygen species at less positive potentials than those required to form oxygen-containing species on the catalyst, several authors also reported the contribution of ceria activity as a structural promoter [27–38].

Nevertheless, on the subject of fuel cell applications, only a few studies have reported cerium oxides as catalyst supports [38–41]. Concerning alcohol oxidation in PEMFCs, Tapan [39] for instance investigated ethanol electro-oxidation on home-made ceria-supported AgCu alloys. They found ethanol oxidation started around 0.2 V (vs. RHE) on CeO_2-supported samples and around 0.4 V (vs. RHE) over Pt disc electrodes, which means that catalysts prepared onto CeO_2 support are the least affected by the strongly adsorbed byproducts. Menéndez [40] designed CeO_{2-x} ($0 < x < 0.5$) nanorods to support electrodeposited Pt nanoparticles (NPs) for short-chained alcohol (methanol, ethanol and *n*-butanol) electro-oxidation in alkaline medium. Tests on unsupported and CeO_{2-x} supported Pt showed that the electrochemically active surface area reduced after anchoring catalyst NPs on ceria, which was ascribed to the low conductivity of the CeO_{2-x}. However, the onset potentials decreased in the corresponding order: Pt > Pt/CeO_{2-x}. The relative enhancement in electrocatalytic activity on Pt/CeO_{2-x} was also confirmed with the chronoamperometric responses. Their results indicate that CeO_{2-x} nanorods are useful for removal of catalyst poisoning. More recently, Altamirano-Gutiérrez [41] carried out a research on the electro-oxidation of formic acid and glycerol in acid medium on Pd–CeO_2. They reported a poor catalytic activity for the formic acid oxidation whereas no activity was observed for the glycerol reaction in comparison to Pd/C. Opposite to that, the authors demonstrated the positive effect of dispersing ceria NPs on carbon black as support. Despite the promotional contribution in electrocatalysis, cerium oxides have been less studied as fuel-cell supports likely due to the worsened electrical conductivity. Better conductive materials are expected to result in less resistance and more efficient electro-oxidation. Considering the intrinsic conduction and bandgap, synthesis of cerium oxides for fuel cell application is still far off.

In this contribution, the effect of crystal growth on cerium dioxide bandgap is discussed and correlated. We investigated the modification of the cerium dioxide electronic structure on the activity and anti-poisoning ability of supported Pt NPs towards ethanol oxidation reaction (EOR), which has been regarded as a cornerstone reaction in exploring the electro-oxidation of green fuels for energy conversion. A relationship between the properties of cerium dioxide and the electrochemical performance of supported Pt NPs was also observed.

2. EXPERIMENTAL

2.1. CeO_2 NPs synthesis

CeO_2 NPs were prepared by a wet chemical precipitation method with cerium(III) chloride heptahydrate (99.9%, Sigma-Aldrich) and ammonium hydroxide (30%, Alphatec) as starting chemicals. Briefly, a 7.4 $mol \cdot L^{-1}$ ammonium hydroxide aqueous solution was slowly dropped into a 0.0175 mol cerium(III) aqueous solution until pH 9.0 under vigorous stirring. The obtained gel was aged for 30 min at room temperature and sequentially washed with deionized water, ethanol (99.7%,

Alphatec) and *n*-butanol (99.4%, Alphatec) repeatedly [42,43]. The gel was then dried at 60 °C for 24 h and ground into a fine powder in an agate mortar. Portions of the dried gel were calcined in air at 400, 600 and 800 °C for 1 h. Samples nomenclature was reported in Table 1.

Table 1. Samples nomenclature, chemical composition, crystallite sizes and optical bandgaps.

Sample	Support nomenclature	Measured element content (wt.%)[a]		Crystallite size (nm)[b]		E_g (eV)[c]
		Pt	Ce	Pt	CeO_2	
Pt/Ce-OD	Ce-OD: oven-dried (60 ºC)	35.8	64.2	5.6	3.7	3.83
Pt/Ce-400	Ce-400: calcined at 400 ºC	35.5	64.5	ND	8.1	3.43
Pt/Ce-600	Ce-600: calcined at 600 ºC	44.1	55.9	6.1	11.9	3.28
Pt/Ce-800	Ce-800: calcined at 800 ºC	36.4	63.6	ND	25.7	3.15

[a]Determined from X-ray microanalysis

[b]Determined from the Debye–Scherrer equation

[c]CeO_2 optical bandgaps estimated from Tauc plots

ND: not determined

2.2. Catalyst NPs synthesis

Pt NPs were anchored on the surface of each synthesized ceria (dried and calcined products) and a commercial carbon black (Vulcan XC72R, Cabot) by a wet chemical impregnation–reduction of chloroplatinic acid (0.05 $g \cdot mL^{-1}$, Sigma-Aldrich) aqueous solution *via* rapid addition of a sodium borohydride (98%, Organics) alkaline solution under vigorous stirring. The amounts of metal precursor were adjusted to a total metal content of 20 wt.%. $NaBH_4$ solutions were prepared in a molar ratio of $NaBH_4$ to Pt metal of 5 [44]. The final mixtures were further stirred for 30 min at room temperature. Resulting products were collected by centrifugation and washed with excess deionized water. Finally, samples were dried at 70 ºC for 2 h and ground into fine powders.

2.3. Materials characterization

Pt and Ce contents in synthesized samples were estimated by X-ray microanalyses (JCM-6000, JEOL) and the nanostructures of supports and supported electrocatalysts were studied using transmission electron microscopy (TEM, JEM-2100, JEOL).

The crystalline structures of as-prepared and calcined ceria powders and supported electrocatalysts were investigated by X-ray diffraction (XRD, Rigaku, Multiflex) with Cu-Kα radiation. Analyses conditions were set at 2θ range 10–90º, step size 0.06º and counting time of 10 sec. For phase identification, the obtained data were compared to ICDD (International Center for

Diffraction Data) cards. The mean crystallite sizes were estimated considering the Debye–Scherrer equation [45]

$$L = k \cdot \lambda / \beta_{2\theta} \cdot \cos\theta \quad (1)$$

where L is the crystallite size, k = 0.89 is the shape factor, λ is the wavelength of the Cu-Kα radiation, θ is the angle at the peak of maximum intensity and $\beta_{2\theta}$ is the full width at half maximum (FWHM) of the corresponding diffraction peak.

Absorbance spectra for as-prepared and calcined cerium dioxides were obtained by ultraviolet–visible absorption spectrophotometry (UV-Vis, Cary 5000, Agilent) in a wavelength ranging from 300 to 800 nm. Optical bandgaps were estimated following the Tauc law [46,47]

$$\alpha \cdot h \cdot v = B \cdot (h \cdot v - E_g)^n \quad (2)$$

where α is the absorption coefficient, h is the Planck's constant, v is the frequency of the radiation, B is a constant, E_g is the average optical bandgap and n is a parameter that depends on the type of electronic transition.

2.4. Electrochemical measurements

Glassy carbon discs (0.196 cm^2, Metrohm Autolab) were used as substrates for the preparation of ultrafine electrodes. 1.6 $mg_{Pt} \cdot mL^{-1}$ aqueous suspensions were produced by ultrasonically dispersing 0.7 mg of a sulfonated tetrafluorethylene based polymer-copolymer (5 wt.% Nafion, DuPont) and 6 mg of each synthesized supported catalysts. A desired aliquot of each suspension was pipetted onto the glassy carbon (GC) substrates, giving a catalyst loading of 0.1 $mg_{Pt} \cdot cm^{-2}$. Electrochemical measurements were performed in a three-electrode cell at room temperature using a PGSTAT302N potentiostat (Metrohm Autolab). Each coated GC was used as a working electrode, whereas a Pt foil as a counter electrode. Potentials were measured in N_2-saturated 0.5 $mol \cdot L^{-1}$ H_2SO_4 (98%, Merck) aqueous solutions and referred to a reversible hydrogen electrode (RHE). The working electrode potential was cycled several times between 0.05 and 0.80 V in order to clean catalyst surfaces. Measurements of the EOR by cyclic voltammetry (CV) were performed after addition of an aliquot of ethanol to yield an alcohol concentration of 1.0 $mol \cdot L^{-1}$. For EOR chronoamperometry (CA), the working electrode potential was held at 0.5 V in N_2-satured electrolyte for 30 min.

3. RESULTS AND DISCUSSION

The phase structures of the final powders were analyzed by XRD (Figure 1).

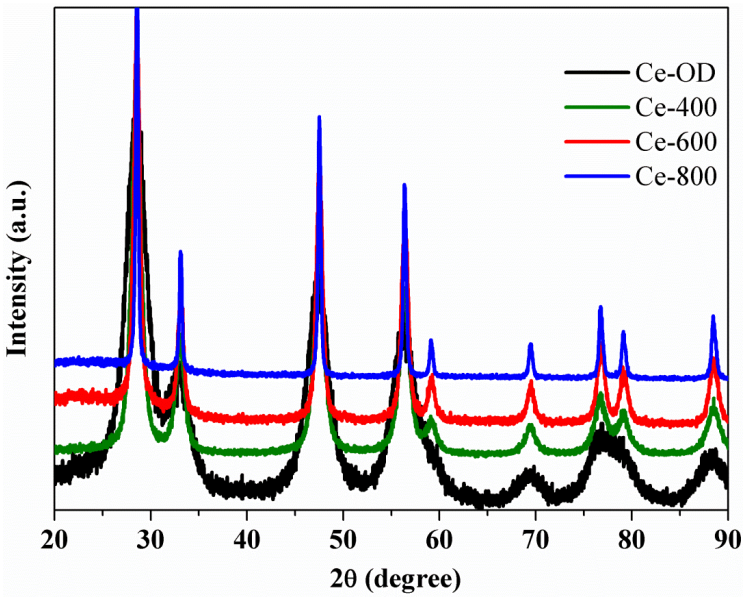

Figure 1. XRD patterns of as-synthesized and calcined cerium dioxide samples. a.u., arbitrary units.

The characteristic peaks of the cubic CeO_2 phase (ICDD PDF No. 78-694) were detected in all XRD patterns. As shown in Figure 1, the change tendency of peaks width suggests an increasing crystallization degree with heating, which can be assigned to an increasing of crystallite size. Following equation (1), further crystallite size determination was carried out (Table 1**)**. As a general rule, crystallite size increased upon heating. The obtained data suggest a reduction in surface-to-volume ratio, resulting in a lower contribution from the surface layer [22]. These could lead to the formation of poorly dispersed catalyst particles, as we should see later.

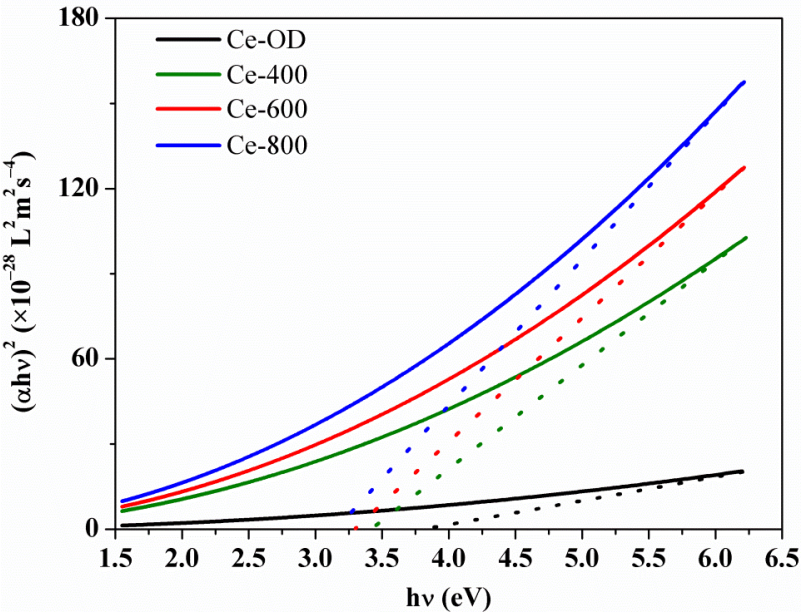

Figure 2. Tauc plots of as-synthesized and calcined cerium dioxide samples. Optical bandgaps were estimated by extrapolating the linear portion of the curves.

Other than high surface-to-volume ratios, a sizeable bandgap is also required for support materials. An estimation of the direct bandgap energies could be obtained from equation (2). Bandgap sizes slightly decreased upon heating (Figure 2 and Table 1), as previously observed by other authors [46–48]. One of the reasons is based on the increasing crystallization degree (Figure 1). As expected, higher intrinsic conduction could be maintained by controlling the structural defects at lower levels, resulting in an increment of electronic mobility. A second explanation is based on crystallite growth (Table 1). This comes from larger number of atoms interacting, which results into split of the energy levels and again incrementing mobility [48]. These indicate therefore a gradual improvement in electronic transport properties with crystal growth.

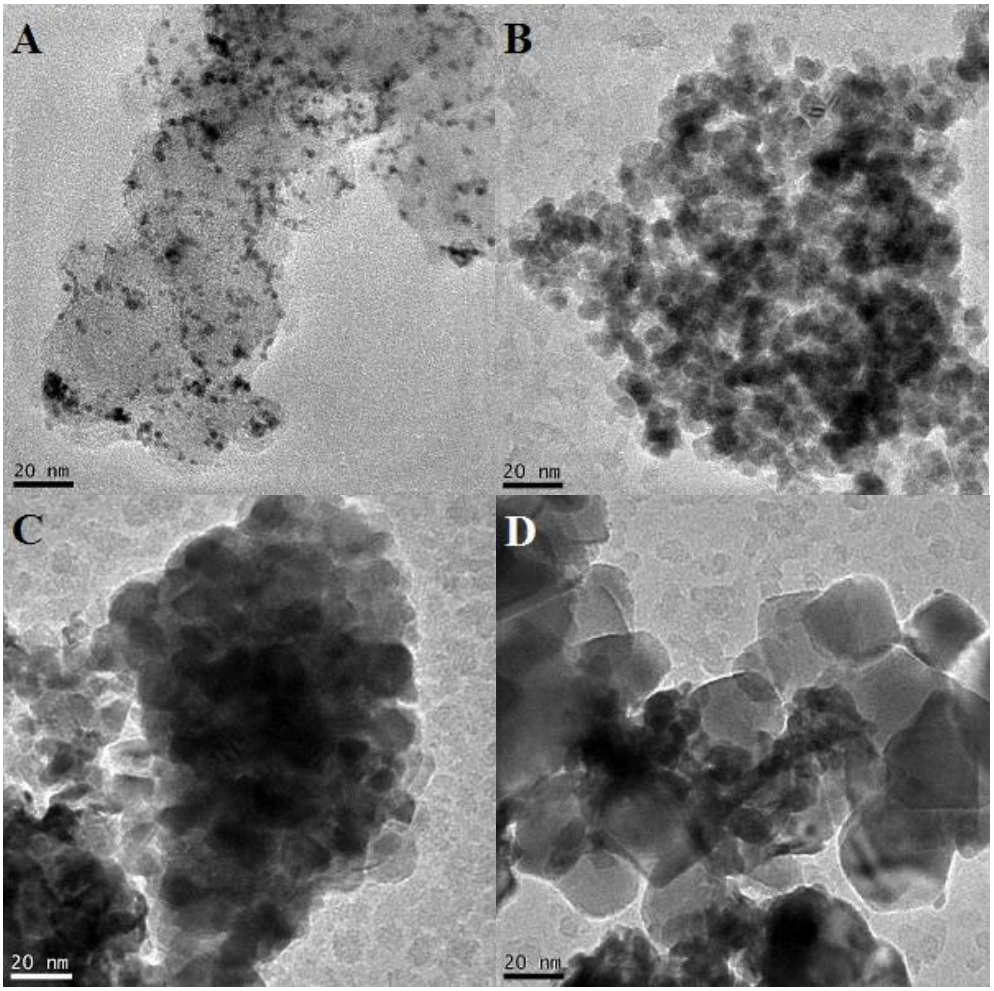

Figure 3. TEM images of Pt NPs supported on Vulcan XC72R (A), Ce-400 (B), Ce-600 (C) and Ce-800 (D).

Particle agglomerates of irregular shape were obtained, as seen *via* TEM (Figure 3, B–D). The formation of aggregated and larger particles implied faster crystal growth upon heating, which was consistent with previous XRD analysis. Pt nanoparticles were poorly dispersed on ceria substrates in comparison to Vulcan XC72R support. The aggregation of Pt NPs onto ceria agglomerates is due to the lower contribution from substrate surface layer to immobilize nanoparticles efficiently. Formation of severely aggregated Pt NPs (Figure 3D) is correlated to the tendency of ceria crystallite growth as

observed from the experimental XRD data (Table 1). These support our hypothesis that lower surface-to-volume ratios substantially weakened metal–support interactions, leading to low control of size, shape and distribution of Pt NPs.

Further structural characterization of the ceria–supported catalysts was carried out with XRD analysis (Figure 4) and considering equation (1). As shown in Table 1, the slight change tendency of average Pt crystallite size (calculated for two selected samples) was used to corroborate our observations.

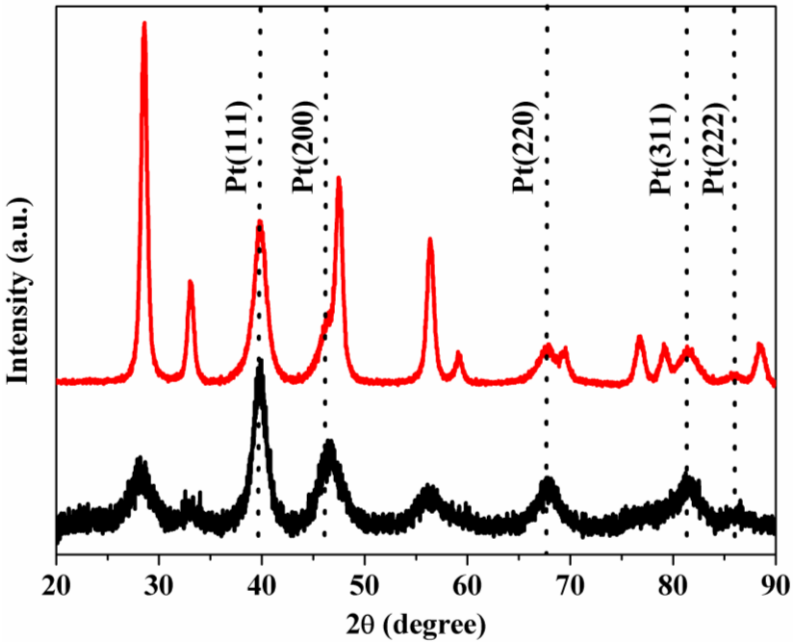

Figure 4. XRD patterns of Pt/Ce-OD (black) and Pt/Ce-600 (red) nanocatalysts. Data were normalized by taking Pt(111) line as a reference. a.u., arbitrary units.

Chemical composition of the synthesized catalysts was summarized in Table 1. Pt and Ce loadings obtained by energy dispersive X-ray analyses were found to be higher (on average, 1.6×) than the nominal values (23.5 wt.% Pt and 76.5 wt.% Ce) for all samples studied. It is proposed the observed differences could be based on a partial reduction of Ce^{4+} to Ce^{3+} in the presence of an excess of sodium borohydride.

The electrochemical characteristics of the supported catalysts were characterized in acid media (0.5 $mol \cdot L^{-1}$ H_2SO_4) by means of a three-electrode cell system. The redox properties of all samples were depicted in Figure 5. It was found that Pt NPs experienced a marked gain in electrochemical activity when ceria crystallite size increased from 3.7 (Ce-OD) to 11.9 nm (Ce-600), from which Pt NPs activity became comparable to that of the state-of-the-art Pt/C/GCE catalyst. This was confirmed with the sharp cathodic current increase from hydrogen adsorption (0.30–0.05 V). When the potential was reversed, the hydrogen desorption took place (0.05–0.30 V) [47]. For small ceria crystals (Ce-OD and Ce-400, $d < 8$ nm), our results mean that Pt NPs could be more easily poisoned by oxygen transported from ceria to catalyst during potential cycling. As previously discussed, the formation of smaller ceria crystals could provide higher surface-to-volume ratios, resulting in stronger metal–support

interactions, enhanced Pt–O binding and fewer free catalytic sites exposed to the solution. The observed influences of crystal growth on hydrogen adsorption/desorption can also be understood from the structure-induced bandgap shrinkage. It is claimed that the increment of electronic mobility in cerium dioxide may also contribute to charge transportation from substrate surface layer to Pt NPs, leading to increased electrocatalytic activity. Cyclic voltammograms of Pt/Ce-400/GCE and Pt/Ce-600/GCE showed a well-defined hydrogen oxidation region (0.05 to 0.30 V) in comparison to other Pt/CeO_2/GCE prepared by borohydride reduction method. This result indicated a higher surface area in comparison with other electrocatalysts prepared, which could contribuite for ethanol oxidation.

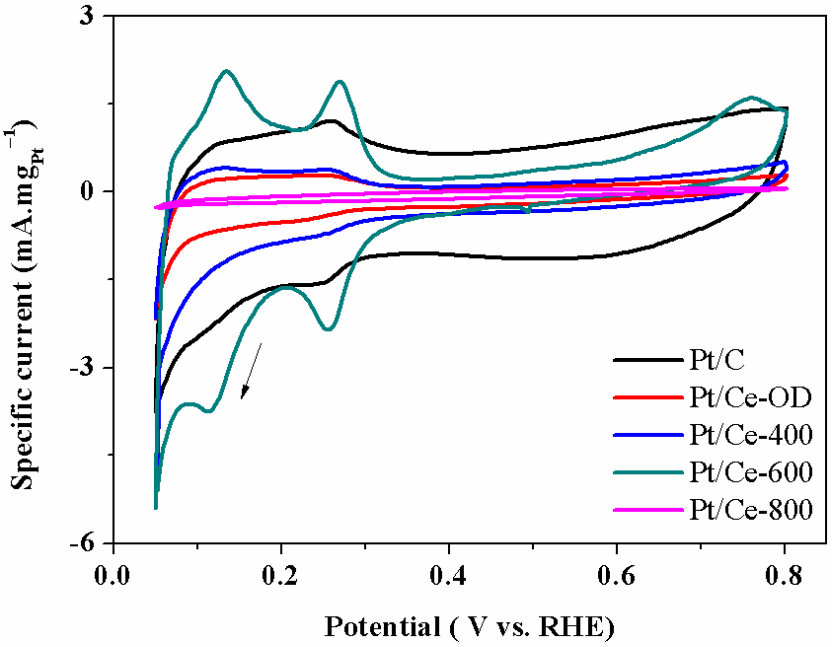

Figure 5. CV curves of catalysts on GC electrode in N_2-saturated 0.5 mol·L^{-1} H_2SO_4 at 25 ºC and a scan rate of 20 mV·s^{-1}, with potential cycled between 0.05 and 0.80 V versus RHE. For all experiments, catalyst loading was fixed at 0.1 mg_{Pt}·cm^{-2}.

On the other hand, Figure 5 illustrates that Pt NPs experienced a significant loss in activity when ceria crystallite size further increased to 25.7 nm (Ce-800). Based on the microstructural features (Table 1 and Figure 3), it can be presumed that the poor control of size, shape and distribution of Pt NPs severely compromised catalyst electrochemical activity, which resulted in inaccessibility of active sites dispersed on support surface layer. From an electronic aspect, the worsened activity could also be attributed to the large crystallite size of cerium dioxide. Generally, in a semiconductor, electron–hole pairs (e^-/h^+) are generated when the electrons in the valence band are excited to the conduction band through some kind of activation (for example, heat, light absorption or an applied electric field) [49]. Therefore, transport efficiency largely depended on the transferring rate of the e^-/h^+ pairs from the bulk to the surface during potential cycling. Despite bandgap shrinkage (Table 1), the growth of cerium dioxide crystals and the increase in diameter might have led to a higher recombination rate because of an increase of the travelling path from bulk to surface.

The EOR activities were determined by CV measurements of the catalysts in an acidic electrolyte (0.5 mol·L^{-1} H_2SO_4) containing ethanol (1.0 mol·L^{-1}). The thermodynamic reversible potential (E^o) of ethanol oxidation at 25 ºC is 0.085 V versus RHE [50]. Any additional potential required to drive the EOR is called the overpotential (η) and, therefore, well-performing EOR catalysts are characterized by low η values, which result from $\eta = E_{onset} - E^o$. The onset potentials (E_{onset}) were determined from the intersection of the two tangents drawn at the current rise and background charging current of the CVs as illustrated in a typical example in Figure 6.

As summarized in Table 2, the EOR activity of the Pt NPs increased with ceria crystallite size. The improved activities were further confirmed by the smaller overpotentials in comparison to that of Pt/C. The inactivity of Pt/Ce-800/GCE catalyst comes as no surprise. Our results confirmed that small cerium dioxide nanocrystals can be efficient EOR catalyst support materials. Furthermore, our ceria-based electrodes demonstrated much better tolerance to the strongly adsorbed EOR byproducts, which could be attributed to the increased ability for transferring electrons to the catalysts, thereby promoting the oxidation of the strongly adsorbed intermediates at lower potentials.

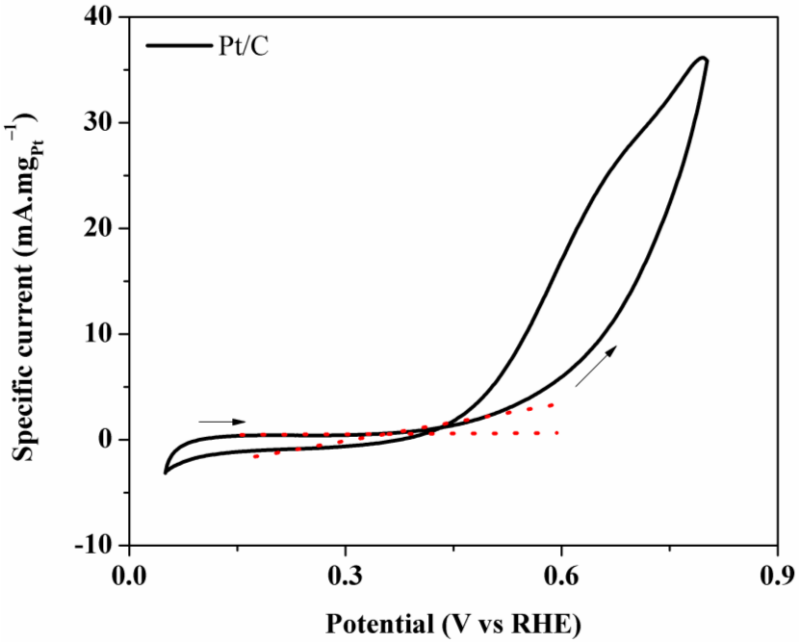

Figure 6. CV curve of 20 wt.% Pt/C catalyst on GC electrode in N_2-saturated 0.5 mol·L^{-1} H_2SO_4 containing 1.0 mol·L^{-1} ethanol at 25 ºC and a scan rate of 20 mV·s^{-1}. Potential was cycled between 0.05 and 0.80 V versus RHE. The onset potential (E_{onset}) was determined from the intersection of the two tangents (red dotted lines) drawn at the current rise and background charging current of the CV. Catalyst loading was fixed at 0.1 mg$_{Pt}$·cm^{-2}.

Additional information on the anti-poisoning ability for EOR of our synthesized Pt NPs was obtained from the dependence of the byproducts-oxidation current on the reaction time (Figure 7). The EOR activities, as determined by CA measurements of the catalysts in an acidic electrolyte (0.5 mol·L^{-1} H_2SO_4) containing ethanol (1.0 mol·L^{-1}) under a fuel-cell relevant potential (0.5 V vs. RHE), were summarized in Table 2.

Table 2. CV and CA results summary of EOR on commercial 20 wt.% Pt/C/GCE and several synthesized 20 wt.% Pt/CeO_2/GCE

Sample	CV results		CA results
	E_{onset} (V)	η (V)	End current ($mA.mg_{Pt}^{-1}$)
Pt/C	0.36	0.27	0.46
Pt/Ce-OD	0.33	0.24	0.23
Pt/Ce-400	0.30	0.21	1.13
Pt/Ce-600	0.28	0.19	0.85
Pt/Ce-800	–	–	–

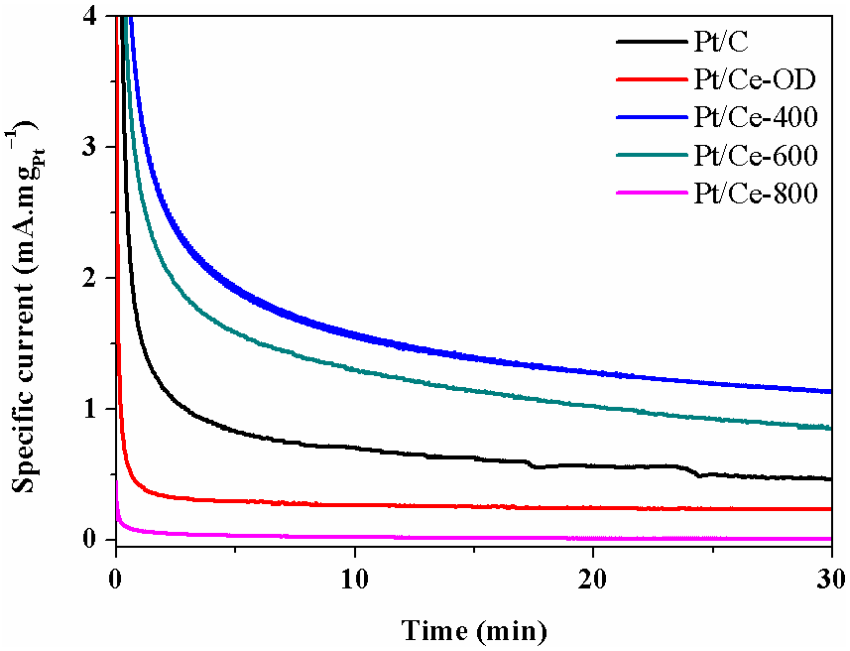

Figure 7. CA (current-time) responses for EOR at a fixed potential of 0.50 V. For all experiments, catalyst loading was fixed at 0.1 $mg_{Pt}·cm^{-2}$.

As time went on, the specific current of the Pt/Ce-OD/GCE and Pt/Ce-800/GCE rapidly decreased in comparison to Pt/C. On one side, deactivation could be understood from the surface layer contribution of the cerium dioxide crystals. Small crystallites (Ce-OD, d = 3.7 nm) could provide enough surface steps, holes, kinks, and terraces for a more effective immobilization of Pt NPs, resulting in a stronger Pt–O binding, whereas large crystallites (Ce-800, d = 25.7 nm) provided a much lower surface layer for NPs anchoring, which led to severe aggregation of the catalysts. In both cases, fewer free active sites were exposed to the solution. On the other hand, deactivation could also be explained based on the electronic contribution of ceria. A wide-gap semiconductor (Ce-OD, E_g = 3.83 eV), despite formed by small crystals (d = 3.7 nm), could offer a higher energetic barrier for donating electrons to the adsorbed EOR byproducts. And large crystals (Ce-800, d = 25.7 nm), despite having smaller bandgaps (E_g = 3.15 eV), could offer a higher recombination rate, which could hamper the transferring of the e^-/h^+ pairs from Pt–CeO_2 interface to the strongly adsorbed EOR intermediates. The

net result is that there are few charge carriers available for reactions at the catalyst surface. As for the comparison of Pt/Ce-400/GCE and Pt/Ce-600/GCE, the former maintained higher specific current from the beginning to the end, probably because the former had suitable crystallite and bandgap sizes, allowing more electrons and holes generated in the bulk to reach to the surface and providing a synergistic effect to create superior electrocatalytic activity and anti-poisoning ability for EOR. Pt/Ce-400/GCE and Pt/Ce-600/GCE showed the highest current values for ethanol oxidation, which could be associated to a higher active surface area and the presence of Ce species. Ce species might have contributed to a bifunctional mechanism. In particular, when considering our synthesized materials for the preparation of large-scale fuel cell electrodes, further research work on tuning the bandgap energy of cerium dioxide is still required. From an electrical aspect, our wide-gap CeO_2 crystals could contribute to a decrement of electron mobility in bulk quantities because a sizeable gap, preferably 0.5–0.7 eV, is required in fuel cells.

4. CONCLUSIONS

Nano-scaled cerium dioxide cubic phase crystals were successfully obtained by a simple and low-cost precipitation method. Increasing crystallization degree and crystal growth were observed due to sintering upon calcination temperature rising. Crystal growth due to sintering was observed by both structural analyses and TEM micrographs. In addition, shrinkage of energy bandgap from 3.83 to 3.15 eV as crystallite size increased from 3.7 to 25.7 nm was verified. Electrocatalysts were prepared and tested for EOR. Our work demonstrated that fine CeO_2 crystals (d = 8.1 nm) contributed better to electro-oxidation on Pt NPs, exhibiting a much higher mass activity (2.5×) than a state-of-the-art Pt/C. The improved activity was attributed to (i) an enhanced metal–support interaction between CeO_2 and metal NPs and (ii) the shrinkage of cerium dioxide bandgap, facilitating electron transportation from Pt–CeO_2 interface to the strongly adsorbed C_xH_y byproducts.

ACKNOWLEDGEMENTS
We would like to thank the Energy and Nuclear Research Institute for supporting this work, especially for the infrastructure of the Materials Science and Technology Center and the Hydrogen and Fuel Cell Center. We would also like to thank our colleagues from XRD, TEM and Lasers and Applications' Multiuser Facilities for the technical assistance.

References

1. K.V. Kordesch and G.R. Simader, *Chem. Rev.*, 95 (1995) 191.
2. T.F. Fuller and M.L. Perr, *J. Electrochem. Soc.*, 149 (2002) S59.
3. O.Z. Sharaf and M.F. Orhan, *Renew. Sust. Energ. Rev.*, 32 (2014) 810.
4. Y. Wang, K.S. Chen, J. Mishler, S.C. Cho and X.C. Adroher, *Appl. Energy*, 88 (2011) 981.
5. A. Brouzgou, A. Podias and P. Tsiakaras, *J. Appl. Electrochem.*, 43 (2013) 119.

6. M.Z.F. Kamarudin, S.K. Kamarudin, M.S. Masdar and W.R.W. Daud, *Int. J. Hydrogen Energ.*, 38 (2013) 9438.
7. O.T. Holton and J.W. Stevenson, *Platinum Metals Rev.*, 57 (2013) 259.
8. Y. Wang, S. Zou and W. Cai, *Catalysts*, 5 (2015) 1507.
9. S.H. Joo, S.J. Choi, I. Oh, J. Kwak, Z. Liu, O. Terasaki and R. Ryoo, *Nature*, 412 (2001) 169.
10. T. Yoshitake, Y. Shimakawa, S. Kuroshima, H. Kimura, T. Ichihashi, Y. Kubo, D. Kasuya, K. Takahashi, F. Kokai, M. Yudasaka and S. Iijima, *Physica B Condens. Matter.*, 323 (2002) 124.
11. C.L. Hui, X.G. Li and I.-M. Hsing, *Electrochim. Acta*, 51 (2005) 711.
12. X. Li and I.-M. Hsing, *Electrochim. Acta*, 51 (2006) 5250.
13. R. Kou, Y. Shao, D. Mei, Z. Nie, D. Wang, C.M. Wang, V.V. Viswanathan, S.K. Park, I.A. Akasay, Y. Lin, Y. Wang and J. Liu, *J. Am. Chem. Soc.*, 133 (2011) 2541.
14. T. Xue, Z.P. Sun, L. Wei, X. Wang and J.-M. Lee J, *Int. J. Hydrogen Energ.*, 38 (2013) 2754.
15. A.O. Neto, M.J. Giz, J. Perez and E.A. Ticianelli and E.R. Gonzalez, *J. Electrochem. Soc.*, 149 (2002) A272.
16. J. Tayal, B. Rawat and S. Basu, *Int. J. Hydrogen Energ.*, 3 (2011) 14884.
17. S.G. da Silva, J.C.M. Silva, G.S. Buzzo, R.F.B. de Souza, E.V. Spinacé, A.O. Neto and M.H.M.T. Assumpção, *Int. J. Hydrogen Energ.*, 39 (2014) 10121.
18. V.V. Pham, V.-T. Ta and C. Sunglae, *Int. J. Hydrogen Energ.*, 42 (2017) 13192.
19. S. Sharma and B.G. Pollet, *J. Power Sources*, 208 (2012) 96.
20. E. Antolini and E.Z. Gonzalez, *Solid State Ionics*, 180 (2009) 746.
21. Z. Zhang, J. Liu, J. Gu, L. Su and L. Cheng, *Energy Environ. Sci.*, 7 (2014) 2535.
22. H. Li, G. Wang, F. Zhang, Y. Cai, Y. Wang and I. Djerdj, *RSC Adv.*, 2 (2012) 12413.
23. M. Mogensen, N.M. Sammes and G.A. Tompset, *Solid State Ionics*, 129 (2000) 63.
24. A. Trovarelli, M. Boaro, E. Rocchini, C. de Leitenburg and G. Dolcetti, *J. Alloys Compd.*, 323-324 (2001) 584.
25. K. Fugane, T. Mori, P. Yan, T. Masuda, S. Yamamoto, F. Ye, H. Yoshikawa, G. Auchterlonie and J. Drennan, *Appl. Mater. Interfaces*, 7 (2015) 2698.
26. L. Yu and J. Xi, *Int. J. Hydrogen Energ.*, 37 (2012) 15938.
27. M. Sedighi, A.A. Rostami and E. Alizadeh, *Int. J. Hydrogen Energ.*, 42 (2017) 4998.
28. M. Priya, S. Kiruthika and B. Muthukumaran, *Ionics*, 23 (2017) 1209.
29. Y. Wang, A. Tabet-Aoul, M. Gougis and M. Mohamedi, *J. Power Sources*, 273 (2015) 904.
30. R.F.D. de Souza, J.C.M. Silva, M.H.M.T. Assumpção, A.O. Neto and M.C. Santos, *Electrochim. Acta*, 117 (2014) 292.
31. M. Wu, M. Han, M. Li, Y. Li, J. Zeng and S. Liao, *Electrochim. Acta*, 139 (2014) 308.
32. Q. Tan, C. Du, Y. Sun, L. Du, G. Yin and Y. Gao, *J. Power Sources*, 263 (2014) 310.
33. M. Lei, T.Z. Yang, W.J. Wang, K. Huang, R. Zhang, X.L. Fu, H.J. Yang, Y.G. Wang and W.H. Tang, *Int. J. Hydrogen Energ.*, 38 (2013) 205.
34. Y. Wei, C. Liu, W. Kang, C. Lai, L. Tsai and K. Wang, *J. Electroanal. Chem.*, 660 (2011) 64.
35. C. Xu and P.K. Shen, *J. Power Sources*, 142 (2005) 27.
36. T. Mori, D.R. Ou, J. Zou and J. Drennan, *Prog. Nat. Sci.*, 22 (2012) 561.
37. A. Lenarda, M. Bellini, A. Marchionni, H.A. Miller, T. Montini, M. Melchionna, F. Vizza, M. Prato and P. Fornasiero, *Inorg. Chim. Acta*, 470 (2018) 213.
38. R. Fiala, A. Figueroba, A. Bruix, M. Vaclavu, A. Rednyk, I. Khalakhan, M. Vorokhta, J. Lavkova, F. Illas, V. Potin, I. Matolinova, K.M. Neyman and V. Matolin, *Appl. Catal. B*, 197 (2016) 262.
39. N.A. Tapan and A. Kök, *Chem. Eng. Commun.*, 196 (2009) 131.
40. C.L. Menéndez, Y. Zhou, C.M. Marin, N.J. Lawrence, E.B. Coughlin, C.L. Cheung and C.R. Cabrera, *RCS Adv.*, 4 (2014) 33489.
41. A. Altamirano-Gutiérrez, A.M. Fernandéz, K.K. Aruna, B. Manoharan, P. Karthikeyan, A. Siller-Ceniceros, P. Meléndez-González, P. Bartolo-Pérez and F.J. Rodríguez-Varela, *J. Appl. Electrochem.*, 45 (2015) 1195.

42. J. Xiao, Y. Wan, H. Deng, J. Li and Y.-X. Liu, *J. Cent. South Univ. Technol.*, 14 (2007) 330.
43. E.S.M. Seo, W.K. Yoshito, V. Ussui, D.R.R. Lazar, S.R.H.M. Castanho and J.O.A. Paschoal, *Mater. Res.*, 7 (2004) 215.
44. M.-S. Hyun, S.-K. Kim, B. Lee, D. Peck, Y. Shul and D. Jung, *Catal. Today*, 132 (2008) 138.
45. A. Velázquez-Palenzuela, E. Brillas, C. Arias, F. Centellas, J.A. Garrido, R.M. Rodríguez and P.-L. Cabot, *J. Phys. Chem. C*, 116 (2012) 18469.
46. H.H. Ko, G. Yang, H.Z. Cheng, M.C. Wang and X. Zhao, *Ceram. Int.*, 40 (2014) 4055.
47. D.M.D.M. Prabaharan, K. Sadaiyandi, M. Mahendran and S. Sagadevan, *Mat. Res.*, 19 (2016) 478.
48. S. Anirban and A. Dutta, *Mater. Res. Bull.*, 86 (2017) 119.
49. P. Avouris, Z. Chen and V. Perebeinos, *Nat. Nanotechnol.*, 2 (2007) 605.